Establishing tungsten carbides as active catalysts for CO2 hydrogenation

Journal:	*Nanoscale*
Manuscript ID	NR-ART-06-2022-003281.R2
Article Type:	Paper
Date Submitted by the Author:	07-Oct-2022
Complete List of Authors:	Juneau, Mitchell; University of Rochester, Chemical Engineering Yaffe, Daphna; University of Rochester, Chemical Engineering Liu, Renjie; University of Rochester, Chemical Engineering Agwara, Jane; University of Rochester, Chemical Engineering Porosoff, Marc; University of Rochester, Chemical Engineering

SCHOLARONE™
Manuscripts

ARTICLE

Establishing tungsten carbides as active catalysts for CO_2 hydrogenation

Mitchell Juneau,[a] Daphna Yaffe,[a] Renjie Liu,[a] Jane N. Agwara,[a] Marc D. Porosoff[a]*

Molybdenum carbides are promising cataysts for the reverse water-gas shift (RWGS) reaction, and we aim to understand if similar performance can be observed across the library of transition metal carbides. Although tungsten and molybenum carbides exhibit similar catalytic properties for hydrogenation reactions, tungsten carbide has not been thoroughly evaluated for CO_2 hydrogenation. We hypothesize that the extreme synthesis conditions necessary for carburizing tungsten can cause sintering, agglomeration, and carbon deposition, leading to difficulty evaluating the intrinsic activity of tungsten carbides. In this work, tungsten is encapsulated in silica to preserve particle size and demonstrate correlations between the active phase composition and RWGS performance.

Introduction

Transition metal carbides (TMCs) are a promising class of materials for CO_2 conversion due to their high activity and controllable selectivity toward C_1 products.[1-3] TMCs achieve comparable hydrogenation activity to precious metal catalysts due to similar electronic properties, but at a fraction of the material cost.[4-7] Recent studies within our group show K-promotion of molybdenum carbide increases CO selectivity via increased CO_2 binding energy and a reduced barrier for CO_2 dissociation,[8, 9] which translates to high performance during reactor studies. K-Mo_2C is active, selective and stable for the reverse water-gas shift (RWGS) reaction at both laboratory (~100 mg) and pilot scales (~1 kg), suggesting viability for future CO_2 to value-added product applications.[10]

Similar studies have been extended to tungsten carbide, another Group VI transition metal carbide, where CO selectivity enhancements are also observed upon alkali metal promotion.[11] Alkali metal promoters increase tungsten dispersion, CO_2 and CO adsorption, and facilitate carburization, suggesting that the alkali metals function as structural and electronic promoters. However, the intrinsic effects of alkali promoters on catalytic properties, and in turn, performance are challenging to isolate.[11]

In general, tungsten carbides demonstrate inferior catalytic activity for CO_2 hydrogenation relative to Mo_2C, even though the two carbides are reported to have similar CO_2 dissociation barriers. This could be a result of both W and Mo carbides exhibiting comparable charge transfer from the transition metal atoms to neighboring carbon atoms.[12, 13] Therefore, we hypothesize the lower activity of tungsten carbides is due to the

low accessibility of active sites caused by particle agglomeration at the high temperatures required for tungsten carburization.[14-17] Several methods of controlling particle size have been reported using reverse microemulsion,[18, 19] and micelle-assisted synthesis methods to support tungsten within a mesoporous silica scaffold.[20-22] The mesoporous silica is hypothesized to stabilize the tungsten particles, preventing agglomeration during high temperature carburization.[20, 23, 24]

During carburization, tungsten oxide is first reduced to tungsten metal, followed by carbon deposition on the catalyst surface, which diffuses into the bulk to form W_2C, followed by the thermodynamically stable WC. Complete carburization is particularly important to ensure inactive tungsten oxides and tungsten metal are carburized to W_2C and/or WC.[6, 25] The hypothesized active W_2C phase has been recently isolated when supported on SiO_2, suggesting that the carburization conditions can be manipulated to synthesize tungsten carbide catalysts with improved control over reactor performance.[15, 26, 27]

Controlling both the tungsten carbide particle size and phase is particularly challenging because the extent of carburization is a function of particle size, resulting in mixed WC, W_2C and WO_x phases at larger particle diameters.[28, 29] Recent computational work indicates that the tungsten carburization pathway is a function of both surface energy and particle size, such that γ-WC and ε-W_2C phases dominate below 10 nm, and the δ-WC is the thermodynamically favored phase at particle sizes above 10 nm.[30] These findings have been validated experimentally, which indicate that isothermal carburization conditions can produce the isolated tungsten semicarbide (W_2C) phase at temperatures below 800 °C at the critical domain size of 10 nm.[31]

In this paper, we aim to isolate the effects of tungsten carbide phase and particle size on CO_2 hydrogenation performance. For studying the effect of particle size, we are contrasting a micelle-based synthesis technique (M) with control experiments over catalysts synthesized by incipient

wetness impregnation (IWI). The effect of carburization is studied by varying the carburization conditions at 600 °C, 835 °C and 1000 °C.[18, 20, 32] Our findings demonstrate that tungsten carbide particles encapsulated within mesoporous silica exhibit increased RWGS activity relative to the IWI controls. The catalysts are stable for 12 hours on stream, despite observed particle agglomeration during the reaction, which suggests the well-dispersed tungsten carbide particles enhance the degree of carburization, and in turn, RWGS performance.

Experimental

Catalyst Preparation

Nano-W_xC (M) was synthesized with a previously reported micelle-based synthesis method,[20] using 168.2 mg of ammonium tungsten oxide hydrate (ATOH, Alfa Aesar), and cetyltrimethylammonium bromide (CTAB, Alfa Aesar) as a soft template, for a theoretical tungsten loading of 15 wt.%. In brief, CTAB was dissolved in water at 80 °C, followed by pH adjustment of the solution to 11.8 with 2 M NaOH before addition of ATOH and tetraethyl orthosilicate (TEOS, Alfa Aesar). After aging the solution for two hours under stirring, the solid was separated by vacuum filtration before drying overnight.

W_xC/SiO_2 (IWI) was synthesized via incipient wetness impregnation of ATOH on SiO_2 (Alfa Aesar, amorphous fumed, S.A. 130-170 m^2/g, 325 mesh powder) with a target loading of 15 wt.% W. Both the M and IWI catalysts were calcined at 550 °C with 2°C/min ramp rates for six hours. All catalysts were carburized using one of the three temperature profiles shown in **Figure 1** in a 21% CH_4/H_2 mixture (33 mL/min of CH_4, 122 mL/min of H_2). After a set time at max temperature (20 hours, 4 hours, and 0.75 hours for Profile 1, 2 and 3 respectively), CH_4 flow was shut off and catalysts were cooled to room temperature under H_2. The catalysts were then passivated under 1% O_2/N_2 (30 mL/min) for three hours.

Transmission Electron Microscopy

Transmission electron microscopy (TEM) of the catalysts were performed in a FEI Tecnai G2-F20 scanning transmission electron microscope operated at an accelerating voltage of 200 kV. The dry powder was directly deposited on the carbon coated copper grid without any pretreatment before transferring the grid into the TEM. Particle size distributions were determined with ImageJ by measuring over 200 particles for all samples.

N₂ Physisorption

N_2 physisorption measurements were performed using a Micromeritics ASAP 2020 BET Analyzer at -196 °C to determine catalyst porosity and surface area. All catalysts were degassed at 350 °C for 2 h under vacuum before analysis.

Pulse Oxidation

Pulse oxidation experiments were used to quantify the active surface area of the catalysts. Pulse oxidation was performed using a Micromeritics AutoChem II 2920, where the catalyst was carburized *in situ* using a premixed 21% CH_4/H_2 gas mixture at 600 °C, 835 °C or 1000 °C, before pulsing probe gas (1% O_2, 99% N_2) ten times over the catalyst at 35 °C.

Inductively Coupled Plasma

Inductively coupled plasma mass spectrometry (ICP-MS) was used to quantify the elemental content of the catalysts. The samples were weighed and digested in aqua regia at 95 °C for one hour. A 1 mL aliquot was taken and diluted to 50 mL with 3% aqua regia. The samples were analyzed on a NeXIOn 2000C ICP-MS in KED mode with FR power at 1600 W with helium flow at 4.2 mL/min. Each sample was run in triplicate.

X-ray Diffraction

X-ray diffraction (XRD) spectra were collected on a Rigaku XtaLAB Synergy-S diffraction system equipped with a HyPix-6000HE HPC detector. CuKα radiation (λ = 1.54184 Å) was generated by a PhotonJet-S microfocus source at 50 kV, 1 mA. At room temperature and with a sample-to-detector distance of 34 mm, two combination ω-φ "Gandolfi" scans were performed, each for 300 s: 1) ω from -62.0 to 31.0 degrees and φ rotated through 720 degrees, at ϑ = 42.1 and κ = 70.0 degrees; 2) ω from -31.0 to 61.0 degrees and φ rotated through 720 degrees, at ϑ = 41.0 and κ = -70.0 degrees. Powder samples were affixed to a nylon loop (0.1 mm ID) with a light coating of viscous oil.

Diffuse Reflectance Infrared Fourier Transform Spectroscopy

Diffuse reflectance infrared Fourier transform spectroscopy (DRIFTS) measurements were performed on a Nicolet iS50 spectrometer (Thermo Scientific) equipped with an MCT/A detector. Approximately 50 mg of catalyst was loaded into a Harrick Praying Mantis™ DRIFTS cell with ZnSe windows and
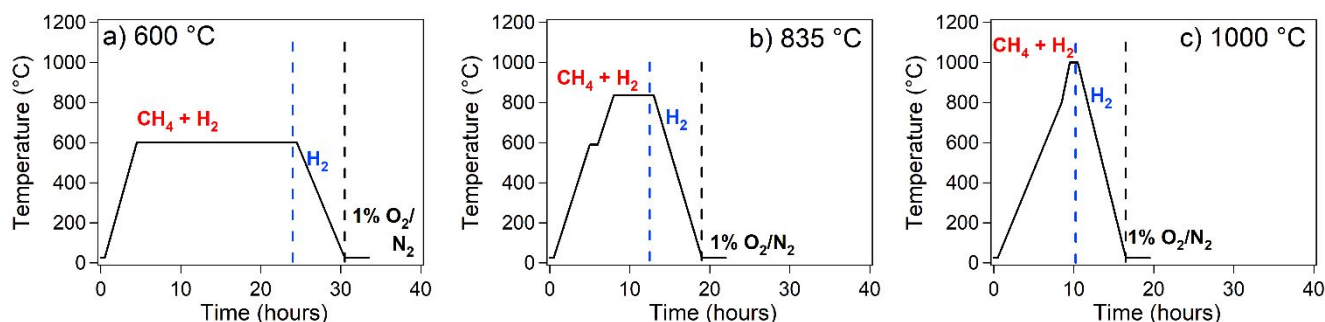

Figure 1. Carburization profiles for M and IWI with a maximum temperature and duration of: a) 600 °C, 20 hours; b) 835 °C, 5 hours; c) 1000 °C, 1 hour.

was reduced at 350 °C for 2 h under a H_2 flow of 7 mL/min. Following reduction, CO_2 was introduced into the cell for 15 min with a 1:1 Ar dilution for a total flow rate of 7 mL/min. Spectra were then recorded after purging gas phase species with Ar.

Packed Bed Reactor Studies

To measure the catalytic performance for RWGS, packed bed reactor studies were performed with 100 mg of catalyst, packed in a 1/4" diameter, 12'' long, stainless steel reactor and reduced under 40 mL/min H_2 for 2 h at 350 °C and 0.34 MPa. After reduction, the reactor was isolated and the bypass pressurized to 2.1 MPa with reactant flow rates of 10 mL/min of CO_2, 30 mL/min of H_2, and 5 mL/min of Ar as an internal standard. Concentrations of reactants and products were analyzed by an in-line Agilent Technologies 7890B gas chromatograph equipped with a flame ionization detector (FID) and a thermal conductivity detector (TCD). The concentration of each gas phase species was calibrated by correlating the peak area of the pure compound to its concentration in a calibration gas standard.

X-ray photoelectron spectroscopy (XPS)

XPS spectra were measured over catalysts using a Kratos Axis Ultra DLD XPS spectrometer equipped with a mono-AlKα X-ray source (1468.6 eV). The spectra were collected using the slot aperture analyzer settings (~300 × 700 μm substrate area). Three sweeps were recorded for the regional scans to increase signal-to-noise ratio. The electron collection angle, θ was zero. Settings for data collection were pass energy: 80 eV, dwell time:

200 ms, energy step size: 0.1 eV. Charge compensation was necessary. Calibration was confirmed with the C 1s peak of carbon tape at 284.6 eV. The XPS signal areas were measured using Casa XPS software with the Shirley background.

W $4f_{7/2}$ binding energies were assigned as follows: W $4f_{7/2}$: W^0 (W metal) at 31.0eV, W^{2+}(W_2C) at 31.5 eV, W^{4+} (WC or WO_2) at 32.4 eV or 32.9 eV and W^{6+} (WO_3) at 36.3 eV.[33-35]

Results

Transmission Electron Microscopy

To confirm effective silica encapsulation of nano-W_xC (denoted as M), TEM images are included in **Figure 2a-c** for the carburized M catalysts. As shown in **Figure 2a**, the W_xC nanoparticles of M 1000 are predominantly 5-20 nm in diameter (median particle size of 6.7 ± 7.3 nm) and distributed within the inner surface and walls of the encapsulating silica shell. Particle size analysis identifies W_xC particles as small as 2 nm, in accordance with values reported previously in literature.[20] Additionally, some aggregates (~25 nm) are observed in the bottom right of **Figure 2a**, illustrating that unbound tungsten carbide particles agglomerate during the high temperature carburization.

Silica encapsulation is also observed over M 835 in **Figure 2b**, but with a wider size distribution than the M 1000 sample, as illustrated by the particle size distribution in **Figure 2e**. In **Figure 2c**, encapsulation of tungsten carbide particles is not observed for the catalyst carburized at 600 °C, and the particle size is the largest of the three samples with median particle size of 15.7 ± 8.4 nm. The observed trend of decreased particle size
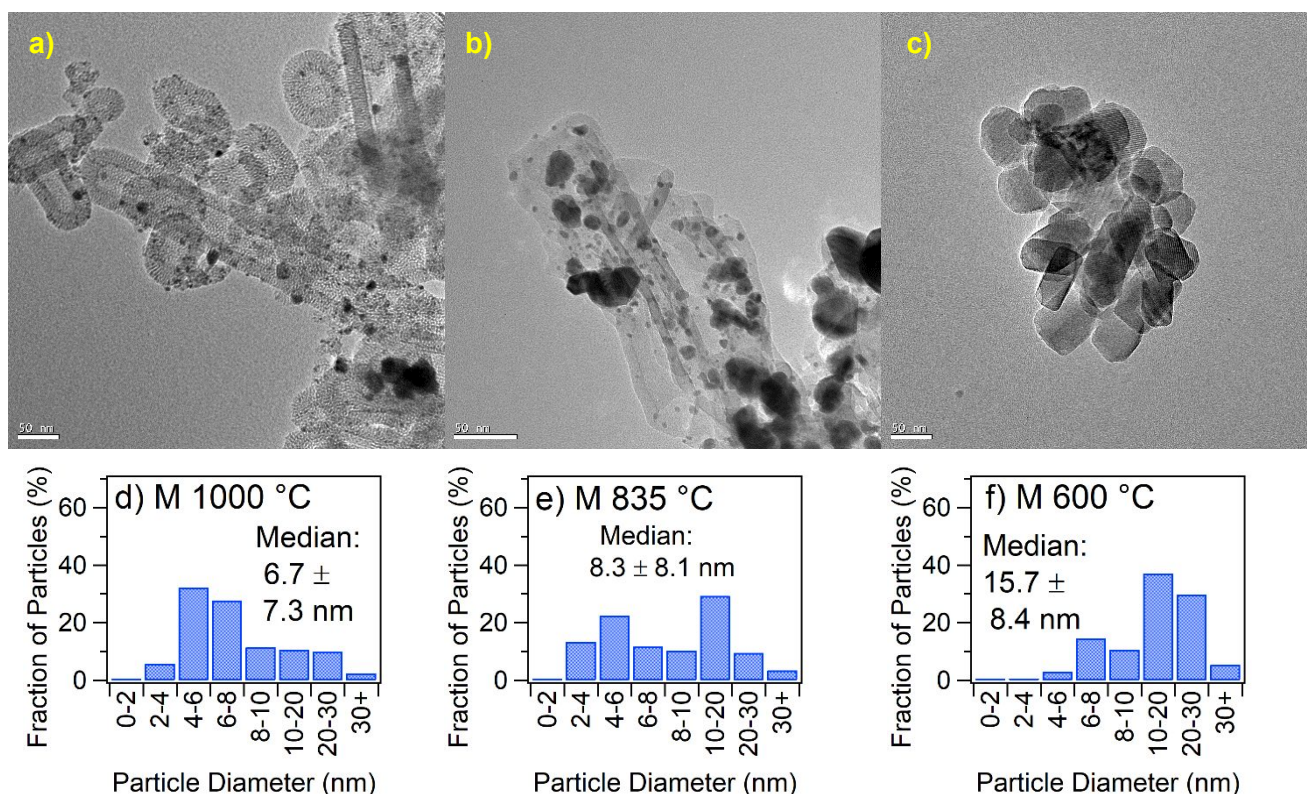

Figure 2. (a-c) TEM images with 50 nm scale bars of nano-W_xC (M) carburized at a) 1000 °C, b) 835 °C, and c) 600 °C, with corresponding particle size distributions (d-f).

and enhanced encapsulation with increasing carburization temperature is supported by the lower BET surface area of M 600 (1.7 m^2/g) relative to M 835 (98 m^2/g) and M 1000 (68 m^2/g). Surprisingly, the data indicates that the median particle size decreases with increasing carburization temperature, suggesting that lower carburization temperatures result in tungsten agglomeration and silica collapse. It is important to note that time of carburization decreases with increasing temperature, with 600 °C, 835 °C and 1000 °C held at their maximum temperatures for 20 hours, 5 hours and 0.75 hours, respectively, as shown in **Figure 1**.

Details on the effect of carburization time are included in **Table S1** and **Figure S1** in the Supporting Information. We observe a bimodal distribution of particle size, with most particles clustered at 4-6 nm and 10-20 nm. While no overall increase or decrease in median or average particle size is observed with increasing or decreasing carburization time, the data in **Figures 2 and 3** suggest that particle size is a complex function of sample preparation, carburization time and maximum temperature.

TEM charactreization of the catalysts synthesized by incipient wetness impregnation (IWI) show formation of large tungsten particles supported on amorphous silica in the TEM images in **Figure 3a-c**. This is further supported by the particle size distribution analysis in **Figure 3d-f**, where IWI 1000 yields a median particle size of 13.0 ± 7.4 nm, larger than the corresponding M 1000 catalyst in **Figure 2a** of 6.7 ± 7.3 nm. In fact, the particle size of the M 1000 and M 835 catalysts are smaller or within error of the IWI catalysts carburized under analogous conditions. In contrast to the M catalysts, BET surface areas of the IWI catalysts appear invariant of carburization

conditions, with surface areas of 128 m^2/g, 173 m^2/g and 112 m^2/g obtained for IWI 600, IWI 835 and IWI 1000, respectively.

The residual sodium present from synthesis of the M catalysts could be affecting the particle size, as sodium has been shown to increase dispersion of tungsten carbides.[11] Quantification of sodium content by ICP-MS indicates all M samples contain 8.0 wt.% Na, which could be a contributor to the decreased particle size of the M catalysts relative to the IWI samples in **Figures 2 and 3**, respectively.

X-Ray Diffraction (XRD)

X-ray diffraction (XRD) patterns in **Figure 4** show a mixed tungsten carbide phase (W$_2$C and WC) with large and discrete peaks observed at 34.6°, 38.0°, 39.6°, 52.3°, 61.9°, 69.8° and 75.1° for W$_2$C, and peaks at 31.4°, 35.7°, 48.4° and 64.4° for WC. These patterns also include features for tungsten oxides at 29.7°, 48.6°, 50.5°, 63.0°, 63.7°, 87.5° and 88.6°, and tungsten metal at 40.3°, 58.3°, 73.1° and 87.1°. PDFs used for peak assignment are: W [PDF:99-933-9427], WC [PDF:99-933-8701], W$_2$C [PDF:99-933-8339] and WO$_3$ [PDF:99-905-0089].

Additionally, while a broad amorphous silica structure is observed over IWI 600 around 20°, carburization at higher temperatures (IWI 835 and IWI 1000) appears to result in restructuring of the amorphous silica support into thermodynamically stable quartz, denoted by the peak at 21.8° (abbreviated as Q). The silica reformation into quartz observed over M 835 is likely occurring during carburization, which is supported by the lower BET surface area observed for the M 835 catalyst, as compared to M 1000 °C. The observed quartz formation for the IWI catalysts carburized at 835 and 1000 °C
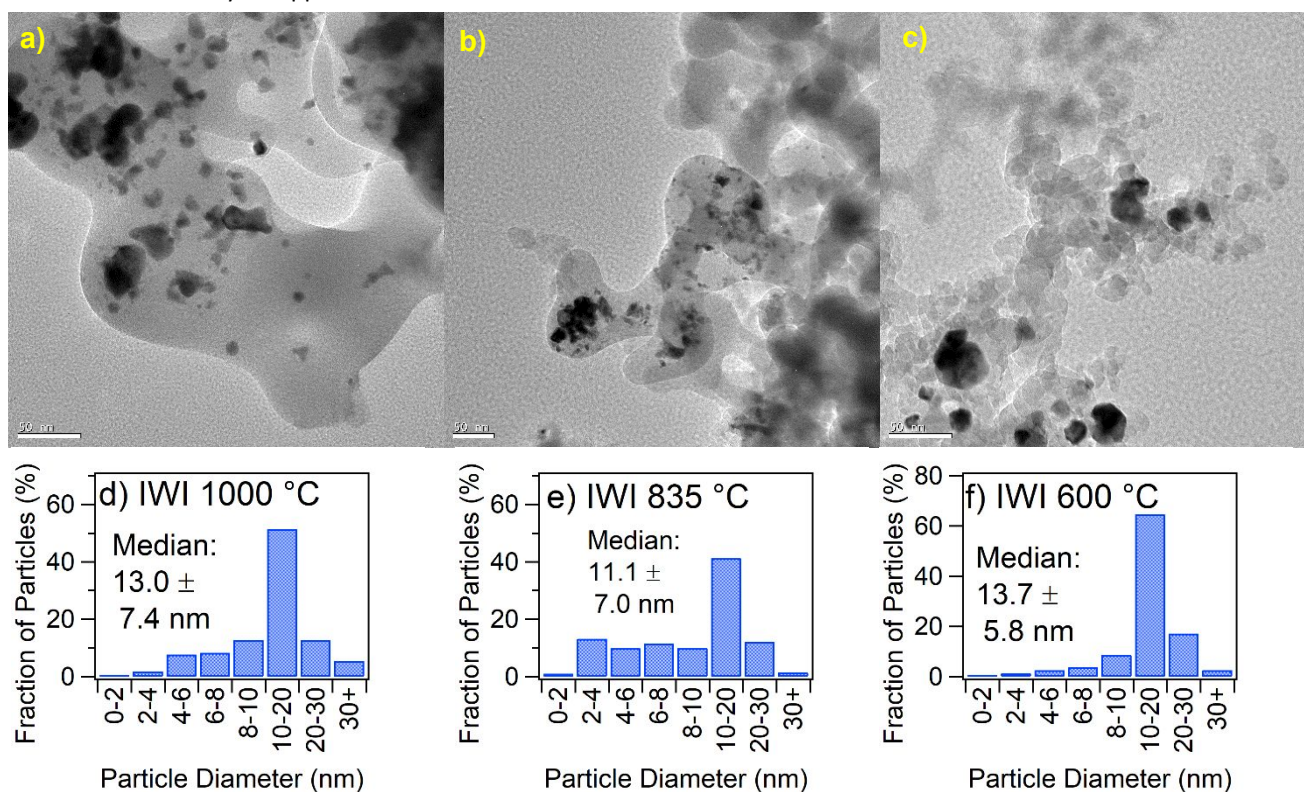

Figure 3. (a-c) TEM images with 50 nm scale bars of IWI W$_x$C carburized at a) 1000 °C, b) 835 °C, and c) 600 °C, with corresponding particle size distributions (d-f).

leads us to hypothesize that high carburization temperatures (> 835 °C) can cause collapse of amorphous silica into thermodynamically stable quartz. We do not observe quartz formation for the M 1000 °C catalyst, likely because of the shorter (0.75 h) carburization time.

Similar high temperature thermal degradation has been reported for analogous SBA-15 and KIT-6 silica-based catalysts. Exposure to temperatures above 800 °C in air results in silica collapse and complete loss of micro and mesoporous surface area, as measured by BET.[36] Additionally, surface area degradation is observed at temperatures as low as 500 °C during air treatment for 5 hours. Therefore, the silica degradation that is observed for the M 600 catalyst during the 20 h carburization (**Figure 1**), could be contributing to the lower surface area observed in BET.

Examining the degree of carburization over the IWI catalysts indicates there is an increasing degree of carburization as a function of temperature, following the proposed carburization pathway of $W \rightarrow W_2C \rightarrow WC$.[37, 38] Careful inspection of the XRD in **Figure 4** reveals that the tungsten metal peak at 58.4° in IWI 600 disappears for the catalysts carburized at higher temperatures, and is replaced with W_2C signatures at 61.9°,

69.7° and 75.1°. At the highest temperature carburization profile (1000 °C) for the IWI catalyst, we observe appearance of peaks at 31.4°, 35.7°, 48.4° and 64.4°, corresponding to WC. Together, the XRD data suggests a greater degree of carburization with increasing temperature, as expected.

Similar trends are observed over the M catalysts, with increasing carbide formation at increasing carburization temperature. More specifically, W_2C peaks are observed in M 835, but the W_2C signatures are virtually eliminated over M 1000, suggesting complete carburization to WC. Interestingly, all catalysts exhibit a large peak at 40.3°, which is attributed to metallic tungsten. This suggests that even at the highest carburization temperature of 1000 °C, the M catalysts did not achieve complete carburization, potentially due to mass transfer limitations from the tungsten nanoparticles encapsulated within silica. Alternatively, because the catalyst precursors are exposed to a CH_4/H_2 mixture during a temperature ramp, the catalyst can be reduced to W metal, which may suppress carbide formation.[17, 27] Furthermore, while W_2C has traditionally been viewed as a thermodynamically unstable carbide phase, recent studies suggest SiO_2 promotes W_2C formation, rationalizing the observed W_2C peaks in IWI 835, IWI 1000 and M 835.[31]
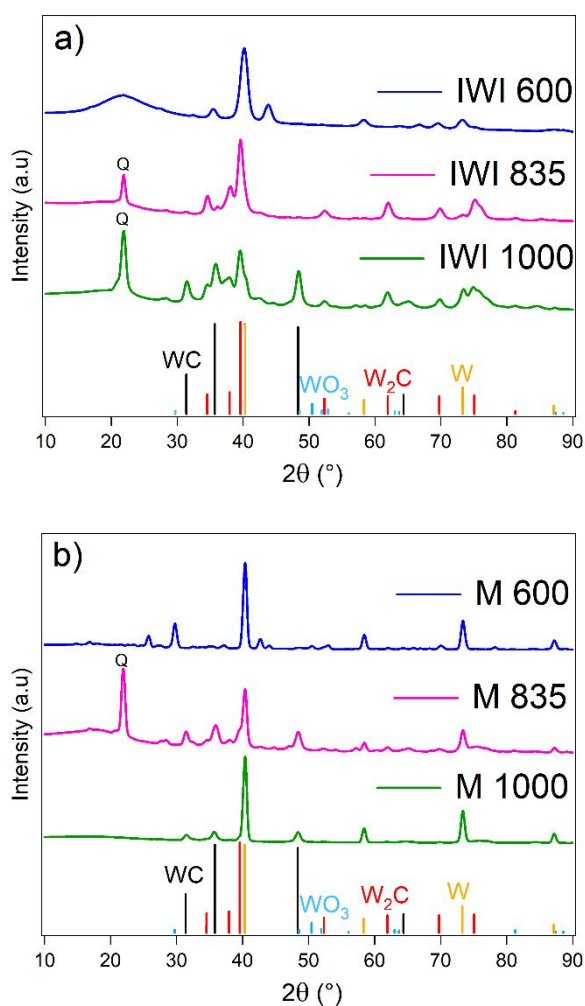
Reactor Studies

Initial activity investigations using diffuse reflectance infrared Fourier transform spectroscopy (DRIFTS) of adsorbed CO_2 over M 1000 and IWI 835 are shown below in **Figure 5**. Both catalysts show a broad peak at 2057 cm^{-1} and sharp peak at 2077 cm^{-1}, attributed to CO linearly bound to carbide species,[5, 39] indicating that CO_2 dissociation is occurring at room temperature. These findings suggest that W_xC-based catalysts are intrinsically active for CO_2 catalysis, in agreement with CO_2 dissociation density functional theory calculations over model WC surfaces.[13]

Packed bed reactor studies for RWGS indicate all catalysts are highly CO selective with methane as the secondary product
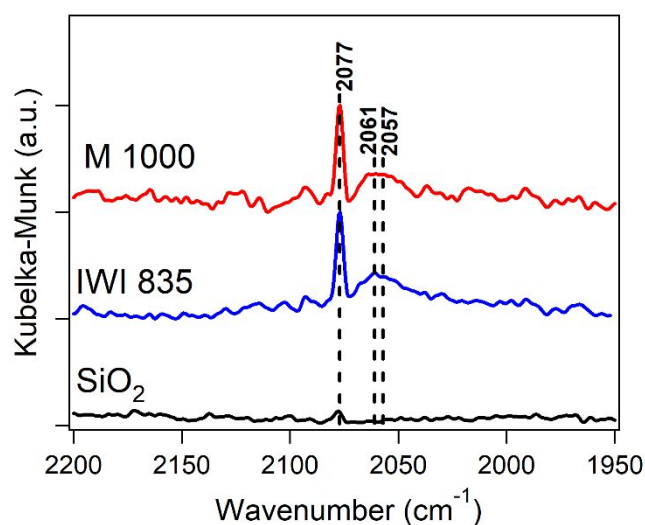

Figure 4. X-ray diffraction patterns of WxC-based catalysts. a) incipient wetness impregnation (IWI) and b) nano-WxC (M).

Figure 5. DRIFTS spectra of reduced M 1000, IWI 835 and bare SiO_2 at 25 °C after CO_2 adsorption. The peaks at 2077 cm^{-1}, 2061 cm^{-1} and 2057 cm^{-1} suggest CO_2 is dissociating into CO.

along with some traces of ethane (<1%). However, as shown in **Figure 6**, the catalysts display varying degrees of activity, represented by CO yield, as a function of time-on-stream. No deactivation is observed over the 12 hours, illustrating all catalysts are stable under RWGS conditions.

From examining the RWGS reactor data in **Figure 6**, M 1000 is the top performing catalyst, with a TOF of 2.9 s^{-1}, significantly improved relative to the IWI 1000 catalyst with a TOF of 1.4 s^{-1}. The differences in reactor performance could be either attributed to the smaller particle size of M 1000 (6.7 ± 7.3 nm) versus IWI 1000 (13.0 ± 7.4 nm) or the composition of the bulk carbide phase. The catalysts carburized at 1000 °C exhibit XRD reflections attributed to WC and metallic tungsten in **Figure 4**, while the IWI 1000 catalyst also contains features attributed to W_2C.

For the M catalysts, the CO yield and activity are functions of the carburization profile, following the trend of M 1000 > M 835 > M 600, which is the same activity trend for turnover frequency (TOF) when the activity is normalized by number of active sites, measured by pulse oxidation in **Table 1**.[40]

Over the IWI catalysts, IWI 835 exhibits the highest RWGS activity, followed by IWI 600 and IWI 1000. However, IWI 835

exhibits the lowest TOF of the IWI catalysts due to the increased O_2 uptake of 6.4 µmol/g. The increased O_2 uptake over IWI 835 could be due to the carburization profile resulting in increased availability of W_xC active sites.

Comparing the TOF values in **Table 1** of the two classes of catalysts shows that the IWI catalysts outperform M 600 but are roughly half as active as M 1000. However, catalysts with similar median particle sizes, for example, M 1000 (6.7 ± 7.3 nm) and M 835 (8.3 ± 8.1 nm), exhibit substantially different activity with respective CO_2 conversions of 13.9% and 4.9%. This suggests that decreased particle size is not the sole factor determining catalytic performance, and that particle accessibility and the surface tungsten carbide phase are likely playing important roles. For example, the low BET surface area of M 600 reported in **Table S2** suggests silica collapse, which agrees with the TEM images in **Figure 2c**, showing tungsten carbide agglomeration within the silica. Lower TOF values over the M 600 and M 835 catalysts could also be from the Na that is present during M synthesis. Details of the BET surface areas are included in **Table S2** of the Supporting Information along with their respective isotherms in **Figures S2** and **S3**.

To further investigate the effect of Na, two controls of IWI 835 and IWI 1000 with 8.0 wt.% Na are included in **Table 1**. While 1 to 3 wt.% Na have been shown to increase CO selectivity at the slight expense of CO_2 conversion over tungsten carbide catalysts, our data suggests that excessive Na appears to diminish activity.[9, 11] Interestingly, M 1000 exhibits the highest conversion and highest TOF of all catalysts, despite the 8.0 wt.% sodium content.

Textural properties are further described through TEM images and particle size distributions after 12 hours time-on-stream (shown in **Figures S4** and **S5** of the Supporting Information) with the summary of particle size distributions included in **Table S3**. Based on the TEM data, particle restructuring occurs under RWGS conditions with median particle size increasing for all catalysts except for IWI 1000 and M 600. All catalysts exhibit stable RWGS activity and stability for 12 hours on stream, suggesting that the particle restructuring occurring under reaction conditions is not a key parameter for determining RWGS activity. Furthermore, as evidenced in the deviations in activity observed over the range of IWI carburization temperatures with little change in particle size, the degree of surface carburization determined by X-ray photoelectron spectroscopy (XPS) is likely playing a key role in the observed activity correlations.
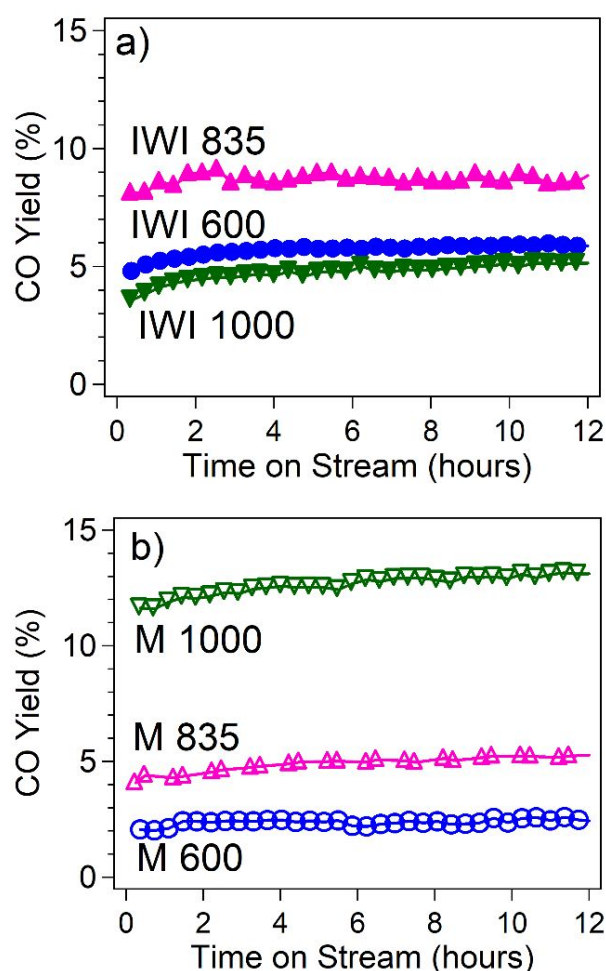

Figure 6. CO yield of W_xC/SiO_2 over 12 hours time-on-stream, synthesized via a) incipient wetness impregnation (IWI), and b) nano-W_xC (M). Experiments are conducted at a GHSV of 27,000 mL/h/g with a 3:1 H_2:CO_2 reactant ratio at 350 °C and 2.1 MPa.

ARTICLE

Table 1. Comparison of performance metrics for W_xC-based catalysts. Packed bed reactor conditions: 3:1: H_2/CO_2 ratio, T = 350 °C, P = 2.1 MPa, and GHSV of 27,000 mL/h/g. Turnover frequency estimated using active site quantification via pulse oxidation model detailed in Supporting Information.

Catalyst	Conversion (%)	Carbon-based Selectivity (%)			CO Yield (%)	O_2 Uptake (µmol/g)	TOF (s^{-1})
		CO	CH$_4$	C$_2$+			
M **600**	2.5	96.5	3.5	0	2.4	2.5	0.6
M **835**	4.9	99.2	0.8	0.0	4.9	2.6	1.1
M **1000**	13.9	94.6	5.0	0.4	13.1	2.7	2.9
IWI 600	6.5	88.0	11.3	0.7	5.7	2.7	1.5
IWI 835	9.2	94.9	4.9	0.2	8.7	6.4	0.9
IWI 1000	5.9	86.3	12.9	0.8	5.1	2.5	1.4
Na-IWI 835	1.3	73.4	25.4	1.2	1.0	--	--
Na-IWI 1000	0.8	95.5	4.5	0	0.8	--	--

Figure 8. Correlation between RWGS activity and XPS contributions of tungsten carbides (W_xC), represented as WC plus W_2C.

X-ray Photoelectron Spectroscopy (XPS)

To gain insight into the active phase and surface structure of the W_xC catalysts, XPS measurements with deconvoluted and quantitative W 4f composition are included in **Figure 7** and **Table 2**, respectively. Reference binding energies for each tungsten species is as follows: W $4f_{7/2}$: W^0 (W metal) at 31.0 eV, W^{2+}(W_2C) at 31.4 eV, W^{4+} (WC or WO_2) at 32.0 eV or 32.9 eV, and W^{6+} (WO_3) at 36.3 eV.[33-35] XPS spectra are collected after the 12 hour RWGS reaction and transferred into the XPS under nitrogen, without exposure to air. For the M 1000 catalyst, a Na 2p peak is observed at ~29 eV, attributed to residual sodium from NaOH added during the synthesis (confirmed as 8.0 wt% from ICP-MS characterization, listed in **Table S5** of the
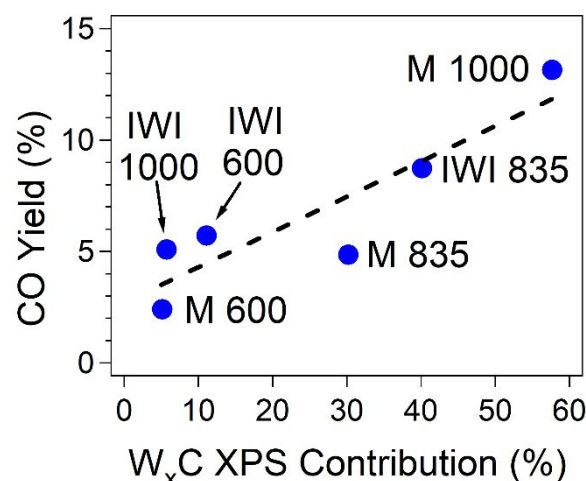
Supporting Information). Peak positions and FWHM are included in **Table S6** of the Supporting Information.

Careful analysis of the quantitative XPS contributions in **Table 2** show that the tungsten metal contributions decrease with increasing carburization temperature for each class of catalyst. The highest degree of tungsten carbide formation (W_2C plus WC) is observed over M 1000 (57.7%), followed by IWI 835 (40.1%), M 835 (30.2%), IWI 600 (11.1%), IWI 1000 (5.7%) and M 600 (5.1%). The RWGS activity follows a similar trend, with M 1000 and IWI 835 exhibiting the highest CO_2 conversion, suggesting that the degree of carbide formation is correlated with activity, as shown in **Figure 8**.[11, 14]

More specifically, M 1000 exhibits the highest degree of W_2C, which may be a result of the intimate contact between the W_xC nanoparticles and the silica support stabilizing the W_2C
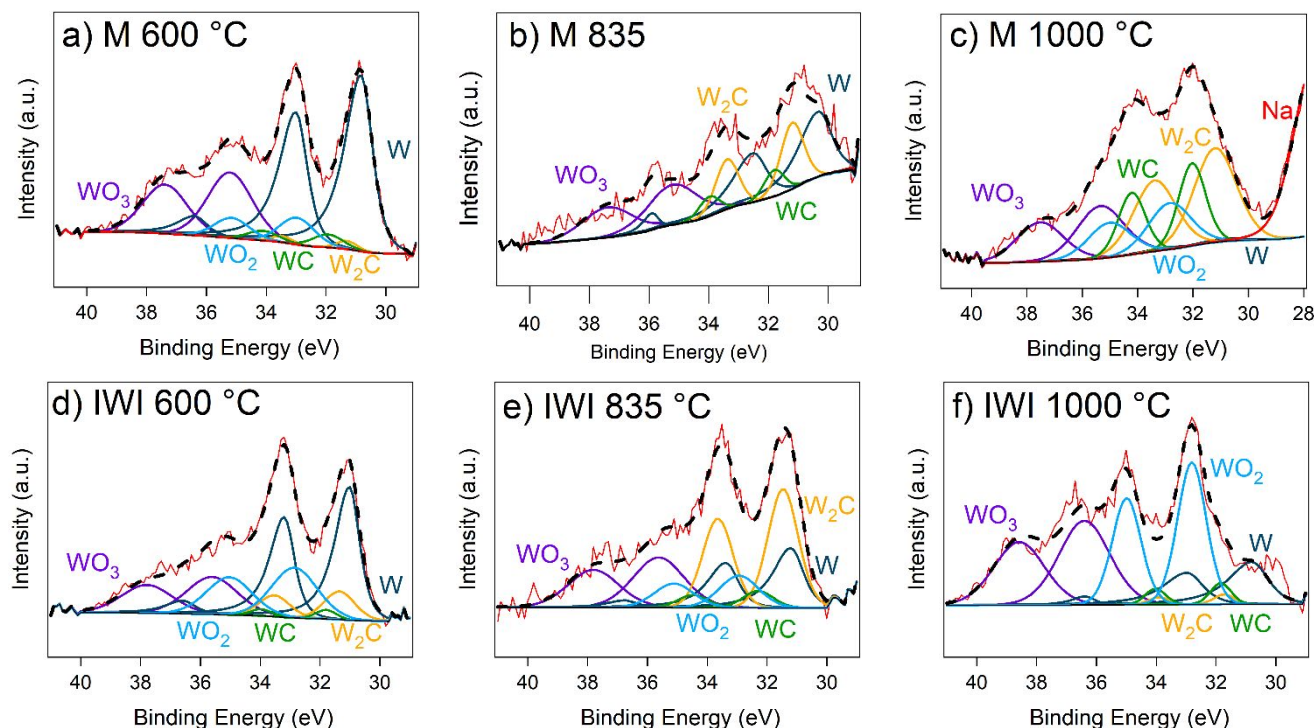

Figure 7. W 4f XPS spectra for W_xC-based catalysts after 12 hours time-on-stream. a) M 600, b) M 835, c) M 1000, d) IWI 600, e) IWI 835 and f) IWI 1000.

phase.[31] The ~10 nm particle diameter of M 1000 may enable formation of a W_2C surface phase, which is not thermodynamically favored at larger particle diameters. This is consistent with the higher degree of W_2C formation over the M catalysts versus the corresponding IWI catalysts in **Table 2**. The increased amount of W_2C could be contributing to the enhanced CO_2 hydrogenation activity over M 1000, as past studies have reported a decreased activation barrier for hydrogenation reactions over W_2C when compared to WC.[26, 41] Additionally, the increased interfacial area of the M catalysts could be responsible for the high selectivity to CO.[42, 43]

Table 2. Deconvoluted W 4f XPS spectra from post-RWGS W_xC catalysts.

XPS Composition (%)	W	W_2C	WC	W_xC	WO_2	WO_3
M **600**	59.0	3.9	1.2	5.1	8.7	27.2
M **835**	40.2	7.8	22.4	30.2	0	29.6
M **1000**	1.3	20.7	37.0	57.7	18.2	22.8
IWI 600	44.8	1.9	9.2	11.1	24.0	20.1
IWI 835	22.8	4.9	35.2	40.1	12.2	24.9
IWI 1000	19.2	3.9	1.8	5.7	36.7	38.4

To contextualize the performance of M 1000 and the other W_xC-based catalysts, **Table S7** of the Supporting Information contains reaction conditions and performance metrics of previously reported transition metal carbides. As shown in the table, M 1000 exhibits a lower CO space-time yield (9.8 μmol CO/g/s) at 350 °C with respect to K-promoted $Mo_2C/γ-Al_2O_3$ (61.4 μmol CO/g/s) and $FeCrO_x$ (85.8 μmol CO/g/s) at 450 °C.[44] Although the performance of M 1000 does not exceed some of the top-performing RWGS catalysts, the CO space-time yield is three times greater than that over previously reported W_xC catalysts (3.2 μmol CO/g/s)[11] and more than five times greater than the M 600 (1.8 μmol CO/g/s) reported in this work. Therefore, the findings of this paper show that the method of synthesizing W_xC-based catalysts is critical for determining their intrinsic activity for CO_2 hydrogenation reactions.

Conclusions

A micelle-based silica encapsulation technique is confirmed to produce ~10 nm tungsten carbide nanoparticles that are promising RWGS catalysts. The high activity and CO selectivity observed over nano-W_xC (M) carburized at 1000 °C is likely due to the encapsulating silica facilitating surface carbide formation by maintaining a ~10 nm particle size during carburization. Preservation of particle size during carburization and intimate contact of the tungsten nanoparticles with the silica support likely promotes formation of active surface carbides (W_xC). When compared to control catalysts synthesized by incipient wetness impregnation, the method of catalyst synthesis is shown to affect the extent of W_xC formation, and in turn, RWGS performance.

Author Contributions

Mitchell Juneau: Investigation, Visualization, Writing-original draft. **Daphna Yaffe:** Investigation. **Renjie Liu:** Investigation. **Jane N. Agwara:** Investigation. **Marc D. Porosoff:** Conceptualization, Supervision, Project administration.

Conflicts of interest

There are no conflicts to declare.

Acknowledgements

Notes and references

1. M. D. Porosoff, X. Yang, J. A. Boscoboinik and J. G. Chen, *Angewandte Chemie*, 2014, **126**, 6823-6827.
2. C. Kunkel, F. Viñes and F. Illas, *Energy & Environmental Science*, 2016, **9**, 141-144.
3. Z. Lin, S. R. Denny and J. G. Chen, *Journal of Catalysis*, 2021, **404**, 929-942.
4. R. B. Levy and M. Boudart, *Science*, 1973, **181**, 547-549.
5. X. Liu, C. Kunkel, P. Ramírez de la Piscina, N. Homs, F. Viñes and F. Illas, *ACS Catalysis*, 2017, **7**, 4323-4335.
6. C. Moreno-Castilla, M. A. Alvarez-Merino, F. Carrasco-Marín and J. L. G. Fierro, *Langmuir*, 2001, **17**, 1752-1756.
7. M. Braun and D. Esposito, *ChemCatChem*, 2017, **9**, 393-397.
8. M. Dixit, X. Peng, M. D. Porosoff, H. D. Willauer and G. Mpourmpakis, *Catalysis Science & Technology*, 2017, **7**, 5521-5529.
9. M. D. Porosoff, J. W. Baldwin, X. Peng, G. Mpourmpakis and H. D. Willauer, *Chemsuschem*, 2017, **10**, 2408-2415.
10. M. Juneau, M. Vonglis, J. Hartvigsen, L. Frost, D. Bayerl, M. Dixit, G. Mpourmpakis, J. R. Morse, J. W. Baldwin, H. D. Willauer and M. D. Porosoff, *Energy & Environmental Science*, 2020, **13**, 2524-2539.
11. J. R. Morse, M. Juneau, J. W. Baldwin, M. D. Porosoff and H. D. Willauer, *Journal of CO2 Utilization*, 2020, **35**, 38-46.
12. J. G. Chen, *Chemical Reviews*, 1996, **96**, 1477-1498.
13. A. A. Koverga, E. Flórez, L. Dorkis and J. A. Rodriguez, *The Journal of Physical Chemistry C*, 2019, **123**, 8871-8883.
14. M. D. Porosoff, S. Kattel, W. Li, P. Liu and J. G. Chen, *Chem Commun*, 2015, **51**, 6988-6991.
15. B. Vidick, J. Lemaître and B. Delmon, *Journal of Catalysis*, 1986, **99**, 428-438.
16. S. M. S. O. Korbag and I. M. S. O. Korbag, *Asian Journal of Green Chemistry*, 2020, **4**, 60-74.
17. H. Lin, B. Tao, J. Xiong, Q. Li and Y. Li, *Ceramics International*, 2013, **39**, 2877-2881.
18. S. T. Hunt, T. Nimmanwudipong and Y. Román-Leshkov, *Angewandte Chemie (International ed.)*, 2014, **53**, 5131-5136.
19. S. T. Hunt, M. Milina, A. C. Alba-Rubio, C. H. Hendon, J. A. Dumesic and Y. Román-Leshkov, *Science*, 2016, **352**, 974-978.

20. Y. Huang, F. Deng, C. Ni, J. G. Chen and D. G. Vlachos, *Dalton T*, 2012, **41**, 6914-6918.
21. Q. Huo, D. I. Margolese, U. Ciesla, P. Feng, T. E. Gier, P. Sieger, R. Leon, P. M. Petroff, F. Schüth and G. D. Stucky, *Nature*, 1994, **368**, 317-321.
22. D. Zhao, P. Yang, D. I. Margolese and G. D. Stucky, *Chem Commun*, 1998, DOI: 10.1039/A804649B, 2499-2500.
23. J. Lemaître, B. Vidick and B. Delmon, *Journal of Catalysis*, 1986, **99**, 415-427.
24. A. K. N. Kumar, M. Watabe and K. Kurokawa, *Ceramics International*, 2011, **37**, 2643-2654.
25. A. Mehdad, R. E. Jentoft and F. C. Jentoft, *Journal of Catalysis*, 2017, **347**, 89-101.
26. B. Vidick, J. Lemaître and L. Leclercq, *Journal of Catalysis*, 1986, **99**, 439-448.
27. A. Löfberg, A. Frennet, G. Leclercq, L. Leclercq and J. M. Giraudon, *Journal of Catalysis*, 2000, **189**, 170-183.
28. L. Hu, S. Ji, Z. Jiang, H. Song, P. Wu and Q. Liu, *The Journal of Physical Chemistry C*, 2007, **111**, 15173-15184.
29. L. Hu, S. Ji, T. Xiao, C. Guo, P. Wu and P. Nie, *The Journal of Physical Chemistry B*, 2007, **111**, 3599-3608.
30. A. Shrestha, X. Gao, J. C. Hicks and C. Paolucci, *Chem Mater*, 2021, **33**, 4606-4620.
31. P. Bretzler, M. Huber, A. A. Rane, R. E. Jentoft, K. Köhler and F. C. Jentoft, *Journal of Catalysis*, 2022, **405**, 60-73.
32. G. Leclercq, M. Kamal, J. M. Giraudon, P. Devassine, L. Feigenbaum, L. Leclercq, A. Frennet, J. M. Bastin, A. Löfberg, S. Decker and M. Dufour, *Journal of Catalysis*, 1996, **158**, 142-169.
33. Y. C. Kimmel, D. V. Esposito, R. W. Birkmire and J. G. Chen, *International Journal of Hydrogen Energy*, 2012, **37**, 3019-3024.
34. M. B. Zellner and J. G. Chen, *Catalysis Today*, 2005, **99**, 299-307.
35. A. Katrib, F. Hemming, L. Hilaire, P. Wehrer and G. Maire, *Journal of Electron Spectroscopy and Related Phenomena*, 1994, **68**, 589-595.
36. J. B. Lowe and R. T. Baker, *Journal of Nanomaterials*, 2014, **2014**, Article 137.
37. G. Mühlbauer, G. Kremser, A. Bock, J. Weidow and W.-D. Schubert, *International Journal of Refractory Metals and Hard Materials*, 2018, **72**, 141-148.
38. K. M. Reddy, T. N. Rao and J. Joardar, *Materials Chemistry and Physics*, 2011, **128**, 121-126.
39. W. Wu, Z. Wu, C. Liang, P. Ying, Z. Feng and C. Li, *Physical Chemistry Chemical Physics*, 2004, **6**, 5603-5608.
40. K. E. Curry and L. T. Thompson, *Catalysis Today*, 1994, **21**, 171-184.
41. K. Isao, M. Eizo, I. Yasunobu and Y. Iwao, *Bulletin of the Chemical Society of Japan*, 1985, **58**, 611-617.
42. I. Ro, J. Resasco and P. Christopher, *ACS Catalysis*, 2018, **8**, 7368-7387.
43. B. Yan, B. Zhao, S. Kattel, Q. Wu, S. Yao, D. Su and J. G. Chen, *Journal of Catalysis*, 2019, **374**, 60-71.
44. M. Juneau, M. Vonglis, J. Hartvigsen, L. Frost, D. Bayerl, M. Dixit, G. Mpourmpakis, J. R. Morse, J. W. Baldwin, H. D. Willauer and M. D. Porosoff, *Energy & Environmental Science*, 2020, DOI: 10.1039/D0EE01457E.